

The miniJPAS survey

Dissecting galaxy properties across environments with spatially resolved photometry

J. E. Rodríguez-Martín^{1,*}, R. M. González Delgado¹, L. A. Díaz-García¹, G. Martínez-Solaache¹, R. García-Benito¹, A. de Amorim², J. Thainá-Batista², R. Cid Fernandes², I. Márquez¹, M. Maturi³, A. Fernández-Soto^{4,5}, R. Abramo⁶, J. Alcaniz⁷, N. Benítez¹, S. Bonoli^{8,9}, S. Carneiro⁷, A. J. Cenarro¹⁰, D. Cristóbal-Hornillos¹¹, R. A. Dupke⁷, A. Ederoclite¹⁰, A. Hernán-Caballero¹⁰, C. Hernández-Monteagudo^{12,13}, C. López-Sanjuan¹⁰, A. Marín-Franch¹⁰, C. Mendes de Oliveira¹⁴, M. Moles^{11,1}, L. Sodré¹⁴, K. Taylor¹⁵, J. Varela¹¹, and H. Vázquez Ramió¹⁰

(Affiliations can be found after the references)

Received 18 August 2025 / Accepted 12 January 2026

ABSTRACT

The Javalambre-Physics of the Accelerating Universe Astrophysical Survey (J-PAS) is an ongoing observational programme aiming to map thousands of square degrees in the Northern Hemisphere. By combining 56 narrow-band photometric filters with a wide field of view, the survey delivers high-quality, integral-field-unit (IFU) like data suitable for investigating both the physical properties and the evolution of galaxies on local scales, as well as the influence of their environment. Preceding this, the miniJPAS survey observed a 1 deg² stripe using the same filter system, serving as a test bench and providing the first scientific results. In this study, we explored the spatially resolved properties of galaxies in miniJPAS and assessed the role of environment in their evolution. Our sample comprises 51 galaxies, classified by spectral type (red or blue) and environment (group or field). We employed our pipeline, Py2DJPAS, to download scientific images and catalogues, mask nearby sources, homogenise the images to the same point spread function (PSF), divide galaxies into regions, and extract their photo-spectra. To analyse the radial profiles of the galaxy properties, we used elliptical annuli in fixed steps of 0.7 R_{EFF} and applied an inside-out segmentation method to investigate their star formation histories (SFHs). The stellar-population properties of these regions are derived using BaySeAGal, a Bayesian parametric code for spectral-energy-distribution (SED) fitting. Additionally, we employed artificial neural networks (ANNs) to estimate the equivalent widths of the key emission lines: H α , H β , [NII], and [OIII]. We find that stellar-population and emission-line properties display clear trends in a colour-mass-density diagram; redder, denser regions tend to be older and more metal-rich, and they exhibit lower specific star formation rates (sSFR), indicating a more quiescent state compared with bluer, less mass-dense regions. These latter regions also show stronger emission lines. While red and blue galaxies are distinctly separated in these diagrams, environmental classification does not produce a similarly clear separation. The radial profiles of the stellar-population properties of the galaxies are consistent with an inside-out formation scenario, based on its SFH analysis. Red and blue galaxies show distinctly different profiles, but we find no significant influence of environment on these properties. We propose that the absence of a strong environmental effect may be attributed to the relatively low stellar mass of the groups in our sample.

Key words. galaxies: evolution – galaxies: fundamental parameters – galaxies: groups: general – galaxies: photometry – galaxies: stellar content

1. Introduction

Surveys using integral field units (IFUs) such as SAURON (Bacon et al. 2001), ATLAS-3D (Cappellari et al. 2011), CALIFA (Sánchez et al. 2012), and MaNGA (Bundy et al. 2015) have significantly advanced our understanding of galaxy properties and evolution. Local processes are thought to drive galaxy evolution (see Sánchez 2020 and Sánchez et al. 2021 for a review). Galaxies, whether disc- or bulge-dominated, show gradients in colour, stellar mass density, stellar age, specific star formation rate (sSFR), and metallicity, typically with higher mass densities and older populations in the central regions, supporting an inside-out formation scenario (e.g. Bell & de Jong 2000; González Delgado et al. 2014, 2015). However, positive age gradients and rejuvenating galaxies have also been observed (e.g. Goddard et al. 2017; Trayford et al. 2016; Tanaka et al. 2024).

In addition to integral-field-unit (IFU) surveys, multiwavelength photometric surveys such as ALHAMBRA

(Moles et al. 2008), J-PLUS (Cenarro et al. 2019), and S-PLUS (Mendes de Oliveira et al. 2019) provide complementary data, enabling detailed analysis of stellar populations. Studies using these surveys have contributed valuable insights into star formation rates (SFRs) and stellar populations in spatially resolved galaxies (see, e.g. San Roman et al. 2018; Logroño-García et al. 2019). These surveys are particularly useful for studying large galaxies that would otherwise be inaccessible due to field-of-view (FoV) limitations (Rahna et al. 2025).

Integral-field-unit-like surveys also reveal how galaxy environment affects evolution. Studies of star formation history (SFH) using techniques such as full spectral fitting (e.g. Pérez et al. 2013; González Delgado et al. 2016) show that galaxy mergers can trigger rapid increases in sSFR, with active galactic nucleus (AGN) driven quenching occurring inside-out and environmental quenching outside-in (Bluck et al. 2020; Lin et al. 2019). Pre-processing in group environments has been shown to alter galaxy properties, with satellite galaxies experiencing enrichment through gas exchange (Schaefer et al. 2019). Moreover, studies by Conrado et al. (2024) highlight differences

* Corresponding author: julioeroma@iaa.csic.es,
julioeroma@gmail.com

in stellar populations and mass densities between galaxies in voids and filaments.

The Javalambre-Physics of the Accelerating Universe Astrophysical Survey (J-PAS, Benítez et al. 2014) is an ongoing survey designed to cover thousands of square degrees in the Northern Hemisphere from the Observatorio Astrofísico de Javalambre (OAJ, Cenarro et al. 2014) using the 2.5 m JST/T250 telescope. Its photometric filter system comprises 54 narrow-band, equally spaced every 100 Å, with a full width at half maximum (FWHM) of ~ 145 Å, plus two medium band filters, u_{JAVA} and J1007, achieving a spectral resolution of $R \sim 60$; this is comparable to very low-resolution spectroscopy over the entire optical wavelength range. The camera's effective FoV is 4.2 deg^2 , and it employs JPCam (JPCam, Taylor et al. 2014; Marín-Franch et al. 2017), a 1.2 Gpixel camera with a pixel scale of $0.23 \text{ arcsec pixel}^{-1}$, using 14 CCDs simultaneously. Prior to this, the miniJPAS survey (Bonoli et al. 2021) covered 1 deg^2 along the AEGIS stripe using the same filter system and providing the first scientific results. This survey was observed using the J-PAS Pathfinder (JPAS-PF) camera equipped with a single CCD, the same J-PAS filter set, and with a low-noise detector of one $9.2 \times 9.2 \text{ k pixel}$. The resulting FoV is 0.27 deg^2 with a pixel scale of $0.23 \text{ arcsec pixel}^{-1}$.

The data from both miniJPAS and J-PAS are ideal for conducting IFU-like studies. Their large FoV allows for the observation of large galaxies within a single pointing, while the filter system enables precise determination of stellar-population properties (see González Delgado et al. 2021; Díaz-García et al. 2024), as well as the estimation of equivalent widths (EWs) for key emission lines (Martínez-Solaache et al. 2021, 2022) and the detection of quasars using machine-learning techniques (Queiroz et al. 2023; Rodrigues et al. 2023; Martínez-Solaache et al. 2023). Furthermore, the survey's design facilitates the detection of clusters and groups without pre-selection bias in the observed targets (see, e.g. Doubrawa et al. 2023; Maturi et al. 2023). This is ensured by the survey's large FoV, which enables the inclusion of all galaxies brighter than the detection limit within the observed area, regardless of their prior classification or known membership. Consequently, the sample is not biased by targeted observations or by pre-selection based on environmental indicators such as colour, morphology, or redshift. In this work, we aim to explore the spatially resolved properties of galaxies in miniJPAS, taking advantage of the capabilities of the J-PAS filter system and the large FoV to investigate the properties of these galaxies and the role of their environment in their evolution. We also demonstrate the potential of future J-PAS data for similar studies.

This paper is structured as follows. In Sect. 2, we describe the nature of the miniJPAS data, as well as the criteria used to select our sample. In Sect. 3, we describe the methodology used for this paper. In Sect. 4, we study the properties of the spatially resolved galaxies in miniJPAS and the role of environment in their evolution, and in Sect. 5 we discuss our results. All the magnitudes used in this paper are given in the AB magnitude system (Oke & Gunn 1983). Throughout this paper, we assume a Lambda cold-dark-matter (Λ CDM) cosmology with $h = 0.674$, $\Omega_{\text{M}} = 0.315$, and $\Omega_{\Lambda} = 0.685$, based on the latest results by the Planck Collaboration VI (2020).

2. Data

The data used in this study come entirely from the miniJPAS survey (Bonoli et al. 2021). In this section, we describe the selection criteria applied to the galaxies included in our sample (Sect. 2.1) and their classification into field and group environ-

ments (Sect. 2.2). The observational and integrated properties of the galaxies in the sample are summarised in Appendix A.

2.1. Sample selection

Galaxies have been selected based on the following criteria: (i) they are at least twice as large as the FWHM of the worst point spread function (PSF), allowing for at least two extractions ($R_{\text{EFF}} > 2''$); (ii) they are not edge-on galaxies (ellipticity must be smaller than 0.6); (iii) they exhibit no artefacts or nearby sources that could bias the photometry ($\text{MASK_FLAGS} = 0$ for all bands, and FLAGS must not include the flag 1); and (iv) the objects are classified as galaxies ($\text{CLASS_STAR} < 0.1$).

With these criteria, we obtained a total of 51 galaxies. These galaxies were subsequently divided into red and blue populations using the selection criterion from Díaz-García et al. (2024), which is an adaptation of the method proposed by Díaz-García et al. (2019a) and previously employed by González Delgado et al. (2021) to separate galaxy populations in miniJPAS into red and blue categories. We classified galaxies as red if they satisfied the following condition:

$$(u - r)_{\text{int}} > 0.16(\log(M_{\star}) - 10) - 0.254 \times (z - 0.1) + 1.689, \quad (1)$$

where $(u - r)_{\text{int}}$ is the intrinsic $(u - r)$ colour of the galaxy, corrected from extinction, and M_{\star} is the total stellar mass of the galaxy, both calculated from SED fitting. Otherwise, the galaxy was classified as blue. According to this criterion, we identified 27 blue galaxies and 24 red galaxies. In Fig. 1, we show some red and blue galaxies, where the differences between the spectral types, such as the different 4000-break amplitudes or the emission lines found in the blue galaxies can be appreciated. The median error of the sample in the MAG_AUTO photometry is 0.026 mag, and it is 0.007 mag for the fits. Consequently, the error bars shown in Fig. 1 are typically smaller than the plotted symbols. The general properties of these galaxies can be found in Appendix A.

2.2. Environmental classification

To study the effects of environment, we further split our sample galaxies into field and group galaxies. For this purpose, we used the adaptation of the AMICO code (Maturi et al. 2005; Bellagamba et al. 2018) developed by Maturi et al. (2023) for the miniJPAS data release. This code is based on the optimal filtering technique (see Maturi et al. 2005 and Bellagamba et al. 2011 for more details), and provides, among other parameters, a probabilistic association of each galaxy with every detected group or cluster.

A key advantage of this approach is that it operates directly on the full, flux-limited galaxy catalogue, without relying on prior knowledge of known clusters or on targeted observations. This ensures that both cluster and field galaxies are identified from the same homogeneous dataset, thereby minimising pre-selection biases related colour or morphology.

This probability has been used in previous studies investigating environmental effects on galaxy evolution (González Delgado et al. 2022; Rodríguez-Martín et al. 2022). Following the same classification as González Delgado et al. (2022), we defined galaxies as group members if their highest probabilistic association exceeded 0.8 and as field galaxies if this value was below 0.1. These thresholds ensure high-purity samples while limiting cross-contamination between environments. Based on this criterion, we identified 15 red field

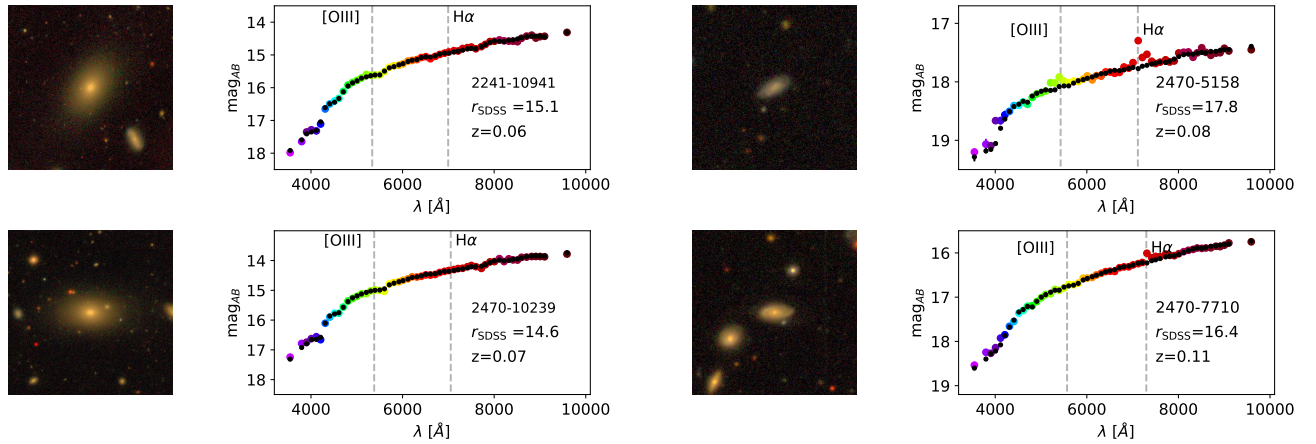


Fig. 1. Example of galaxies in sample and their J-spectra. Left panels show the RGB images of two red galaxies. The second column shows the MAG_AUTO J-spectra of the red galaxies. The third column shows the RGB images of two blue galaxies. Right panels show the MAG_AUTO J-spectra of blue galaxies. Colour points represent the observed magnitudes. Black dots represent the result of the SED fitting. The dashed grey lines represent the wavelengths at which [OIII] and H α are found. Galaxy spectra are shown in the observer frame, and they correspond to the galaxy in the centre of the image. The redshifts shown correspond to the most likely value (PHOTOZ) of the redshift probability density function (zPDF; see [Hernán-Caballero et al. 2021](#)).

galaxies, 21 blue field galaxies, nine red group galaxies, and six blue group galaxies. Following the classification scheme used in other works such as [Yang et al. \(2007, 2009\)](#) and [Bluck et al. \(2020\)](#), where the central galaxy is defined as the most massive galaxy within a dark-matter halo. Similarly, we can use the list of brightest group galaxies (BGGs) provided by [Maturi et al. \(2023\)](#), considering these as the central galaxies of their respective groups. Adhering to this definition, we found a total of eight galaxies that are the BGGs in their groups. However, given the already limited sample size, we chose not to incorporate this classification in our analysis, as it would reduce the number of galaxies in each category even further. This will be taken into account in future work.

3. Methodology

In this section, we summarise the methods and codes used for the analysis of our data. Our methodology is mainly based on three codes: Py2DJPAS ([Rodríguez-Martín et al. 2025](#)), a python tool used to automatise the steps required to obtain the photometric spectra (J-spectra) of the regions of galaxies (Sect. 3.1); BaySeAGal ([González Delgado et al. 2021](#)), the code for spectral-energy-distribution (SED) fitting used to estimate the properties of the regions (Sect. 3.2); and the artificial neural networks (ANNs) trained by [Martínez-Solaache et al. \(2021\)](#) and used to estimate the EWs of the main emission lines (Sect. 3.3).

3.1. Py2DJPAS

The Py2DJPAS code is our custom code developed to streamline and automate the full process required to study spatially resolved galaxies in J-PAS. In brief, it begins by downloading the scientific images and tables necessary for the analysis, including key parameters such as galaxy coordinates, zero points, and photometric redshifts (photo- z). It then masks nearby sources using both the default masks provided in the J-PAS database and additional custom masks that we generate, including deblended sources.

We adopted $NPIX = 10$ and $rms = 5$, where $NPIX$ is the minimum number of pixels for a detection to be considered valid, and rms defines the threshold level for pixel detection. These values strike a good balance between effectively masking nearby contaminants and preserving the genuine background structure (see [Rodríguez-Martín et al. 2025](#)). Next, it convolves all images to match the FWHM of the worst PSF using a Gaussian approximation. This step avoids introducing artificial colour gradients in the photometry (e.g. [Michard 2002](#); [Cypriano et al. 2010](#); [Molino et al. 2014](#); [Liao & Cooper 2023](#)) and is commonly applied in similar analyses (see, e.g. [Bertin et al. 2002](#); [Darnell et al. 2009](#); [Desai et al. 2012](#); [San Roman et al. 2018](#)).

In the final step, the galaxy regions are defined, and the J-spectra are computed for each one. We implemented three segmentation strategies. (i) The first is maximum-resolution segmentation, where we have elliptical rings with a major axis equal to the FWHM of the worst PSF. Rings are added until the median signal-to-noise ratio (S/N) drops below 10. (ii) The second is fixed-step segmentation. Elliptical rings have steps of $0.7 \times R_EFF$, which is the size of the FWHM of the worst PSF compared with the respective galaxy in the sample. (iii) Finally, we used inside-out segmentation, whereby two regions are defined: an inner region ($a \leq 0.75 R_EFF$) and an outer region ($0.75 < a \leq 2 R_EFF$); a is the semi-major axis. This method is used to analyse SFHs (see Sect. 4.4). Only regions with a median S/N greater than 5 in filters with pivot wavelengths of $\lambda_{pivot} < 5000 \text{ \AA}$ are included in the analysis. This criterion was motivated by the strong correlation between the 4000 Å break and the stellar-population properties of galaxies (see, e.g. [González Delgado et al. 2005](#)). Our results show that, for each filter, apertures meeting this S/N threshold yield residuals well below a relative difference of 10%, leading to more accurate fits. In contrast, when measurements in a given filter fall below this threshold, residuals increase substantially, often exceeding 10%, and there is a systematic underestimation of the observed flux (see [Rodríguez-Martín et al. 2025](#)). Hence, this restriction is applied. The median number of regions per galaxy produced by the maximum-resolution segmentation is six, both before and after applying the S/N criterion. For the fixed-step segmentation, the corresponding median is six regions per galaxy

prior to the S/N cut, and five regions per galaxy once the cut is applied. The median error of the measurements is 0.07 mag for the homogeneous ring segmentation, and 0.06 mag for the maximum-resolution segmentation. The median error of the fits is 0.015 mag for both segmentations. After applying the S/N threshold, the median errors decrease to 0.06 mag for the measurements and 0.013 mag for the fits, again for both segmentations.

3.2. J-spectra fits

To obtain the SED fitting for the regions of the galaxies, we utilised BaySeAGal (González Delgado et al. 2021), a parametric SED-fitting code that employs a Markov chain Monte Carlo (MCMC) approach to explore the parameter space. This method generates a sample of parameters that approximate the probability density function (PDF) of the model. In this study, we adopted the same τ -delayed SFH model as that used in González Delgado et al. (2021, 2022) and Rodríguez-Martín et al. (2022).

We retrieved the following parameters: t_0 (the time when star formation commenced, in look-back years), τ (the timescale over which star formation is spread), stellar extinction (A_V), stellar metallicity (Z), and stellar mass (M_*). We also calculated the mass-weighted and light-weighted ages, rest-frame colours, and SFRs. We retrieved the parameters t_0 , τ , Z , and A_V via marginalisation, taking advantage of the Bayesian framework. To account for extinction, the model spectra were attenuated by a factor of $e^{-q_\lambda \tau_V}$, where τ_V is the dust attenuation parameter in the V band and $q_\lambda \equiv \tau_\lambda / \tau_V$ represents the reddening law. In this work, we adopted the attenuation law of Calzetti et al. (2000), which assumes a single foreground screen with a fixed value of $R_V = 3.1$. We used an uniform prior, with the following range of values to look for the solution: $t_0 = [0, 0.99]$ (in units of the age of the Universe, taken from z), $\tau = [0.1, 10]$ Gyr, $A_V = [0, 2]$ mag.

In Fig. 1, we show the quality of the fittings obtained with this code. The models used for the fitting are the version of the Bruzual & Charlot (2003) stellar-population synthesis models updated by Plat et al. (2019). As these models do not include emission lines, the fit is constrained by the stellar continuum, leading to the expected differences between observed and modelled magnitudes in the filters affected by line emission, as seen in Fig. 1. For this reason, we relied on ANNs to estimate the EWs of the relevant emission lines.

3.3. ANNs for emission lines

To estimate the emission-line properties, we utilised the ANN trained and applied by Martínez-Solaache et al. (2021, 2022). The ANN used here was specifically trained to predict the EWs of $H\alpha$, $H\beta$, [NII], and [OIII]. The input layer of the network took the colours of all the filters relative to the filter where $H\alpha$ is observed. To account for redshift, separate ANNs were trained for each redshift value, ranging from $z = 0$ to $z = 0.35$ with a step size of 0.001. The hidden layers optimised the loss function, and the output layer provided estimates for the EWs of $H\alpha$, $H\beta$, [NII], and [OIII].

The ANN model was trained by means of spectra from the MaNGA and CALIFA surveys, convolved with the filters of miniJPAS to simulate synthetic J-spectra. The spectra spanned various regions with different characteristics, including star-forming, quiescent, and AGN regions, ensuring that the ANN is trained across a broad range of galaxy types and conditions. This

diversity improved the accuracy of the ANN predictions for different galaxy types or regions under study. For a detailed description of error handling and missing data, we refer the reader to the original work by Martínez-Solaache et al. (2021). The results of that work indicate that the EWs of $H\alpha$, $H\beta$, [NII], and [OIII] in SDSS galaxies can be estimated with a relative standard deviation of 8.4%, 13.7%, 14.8%, and 15.7%, respectively, and relative biases of 0.03%, 5.0%, 4.8%, and -6.4% , respectively. In addition, the [NII]/ $H\alpha$ ratio is constrained within 0.092 dex with a bias of -0.02 dex, while the [OIII]/ $H\beta$ ratio shows no bias and a dispersion of 0.078 dex in SDSS galaxies. Furthermore, this methodology was also employed by Martínez-Solaache et al. (2022) in order to retrieve the cosmic evolution of the SFR density, which was found to be in agreement with previous measurements based on the $H\alpha$ emission line.

4. Results

This section presents the spatially resolved stellar-population properties (Sect. 4.1), radial profiles of stellar-population parameters (Sect. 4.2), emission-line profiles (Sect. 4.3), and a comparison between the SFHs of inner and outer regions (Sect. 4.4). To streamline the discussion, we define the key properties and units used throughout this section. For clarity, units are not repeated in the text. The main properties analysed are (i) stellar-surface mass density, μ_* , measured in $M_\odot \text{pc}^{-2}$ (we generally refer to its logarithmic value); (ii) mass-weighted stellar age, $\langle \log \text{age} \rangle_M$, expressed in years (logarithmic scale); (iii) mass-weighted stellar metallicity, $\langle \log(Z/Z_\odot) \rangle$; (iv) visual extinction, A_V , given in magnitudes (AB system); and (v) sSFR, in units of Gyr^{-1} (we typically refer to its logarithm).

4.1. Spatially resolved properties

We begin our analysis by introducing a diagram analogous to the stellar mass-colour diagram, which we corrected for extinction (Díaz-García et al. 2019a), substituting stellar mass with stellar mass surface density. To ensure a balanced representation of data points across the diagram, we applied a fixed-step segmentation method (see Fig. 2). This approach yields a well-defined distribution of stellar-population properties. To aid the interpretation of these diagrams, we note that the median uncertainties of the displayed properties are as follows: 0.15 dex for the mass-weighted age, 0.19 mag for the extinction A_V , 0.39 dex for the stellar metallicity, and 0.11 dex for the sSFR.

Older regions are found in the redder and higher surface-mass density parts of the diagram, while younger regions appear bluer, particularly in areas of lower stellar-surface mass density. Interestingly, the highest dust extinctions are observed in the blue regions of high stellar surface mass density. On the other hand, the lowest metallicities are found in the blue areas of low stellar surface-mass density, whereas some of the most metal-rich regions correspond to blue but dense regions. These points are also associated with regions of higher extinction. A dust-metallicity degeneracy might be taking place, although the values for these points remain below the maximum allowed during the SED-fitting process. Furthermore, there is no corresponding increase in the age of these regions, which could have been an alternative parameter for the code to use in reddening the fitted spectra. However, the primary source of uncertainty in these considerations stems from the significant uncertainty in the metallicity values. Overall, redder and denser regions tend to be more metal-rich. These results are in agreement with the radial profiles found in the literature (see, e.g. González Delgado et al.

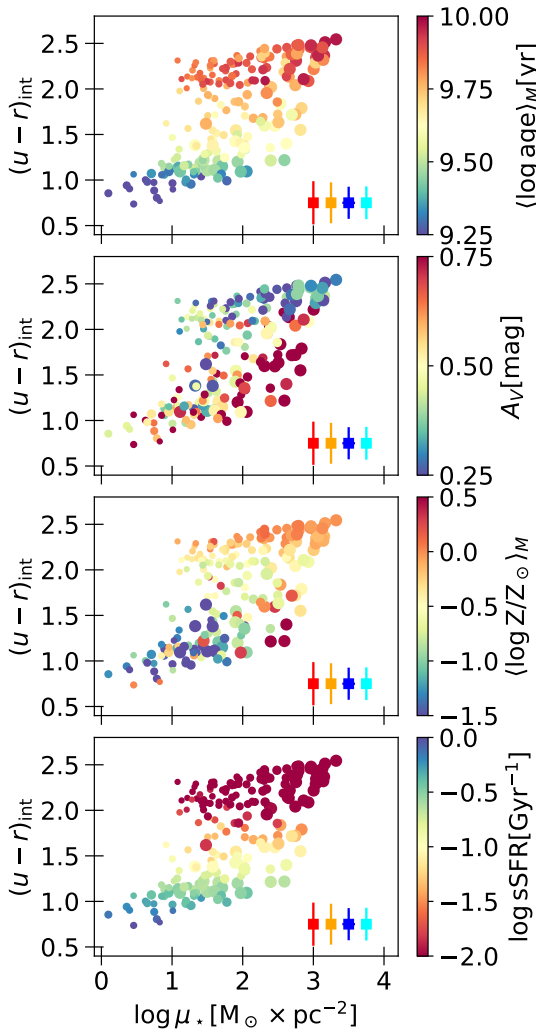


Fig. 2. Colour-mass-density diagram colour-coded by main stellar-population properties. Each point represents a region. From top to bottom: mass-weighted age, extinction, stellar metallicity, and sSFR. Each point represents a different aperture. The squares represent the typical error along each axis colour for each type of galaxy: red galaxies in the field (red), red galaxies in groups (orange), blue galaxies in the field (blue), and blue galaxies in groups (cyan). Point size is inversely proportional to the distance from the galactic centre.

2014, 2015, 2016; San Roman et al. 2018; Bluck et al. 2020; Parikh et al. 2021; Abdurro’uf et al. 2023), since the stellar mass surface density decreases steeply with the radial distance. In this regard, galaxy regions with a high stellar mass surface density can be expected to be closer to the centre. It is precisely in the innermost regions where the oldest and more metal-rich stellar populations, particularly for redder galaxies, are usually found. This also aligns with results shown in our diagrams.

Regions that are both red and dense exhibit the lowest sSFR, suggesting they are the most quiescent, in agreement with the radial profiles of surface mass density and sSFR reported by González Delgado et al. (2015, 2016) and Bluck et al. (2020). Broadly speaking, these diagrams reproduce the same relationships observed in stellar mass-colour diagrams based on galaxies’ integrated properties (e.g. Díaz-García et al. 2019a; González Delgado et al. 2021, 2022; Rodríguez-Martín et al. 2022), implying once the colour, extinction, and stellar mass sur-

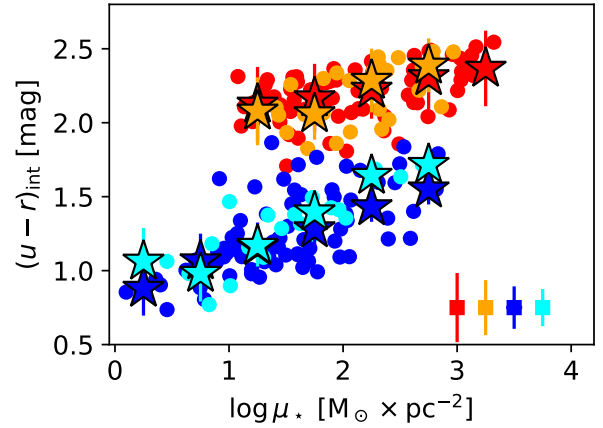


Fig. 3. Colour-mass-density diagram coloured by environment and colour of galaxies. Red points represent regions belonging to the red galaxies in the field. Orange is used for the regions of the red galaxies in groups, blue points are for the regions of blue galaxies in the field, and cyan points are for regions of blue galaxies in groups. Stars represent the median value for each galaxy type in each mass-density bin. Squares represent the same as in Fig. 2.

face density of a given region in a galaxy are known, its other stellar-population properties can be reliably constrained.

Although both colour and mass density correlate with stellar-population properties, colour appears to be the stronger predictor, given the mostly vertical gradient in the diagrams, particularly for the stellar age and the sSFR. This aligns with the results of Díaz-García et al. (2019a), who, using τ -delayed SFHs from Madau et al. (1998) to model galaxies in the ALHAMBRA survey, found that galaxy properties correlate most strongly with colour, but also with size (Díaz-García et al. 2019b). Our findings support this, demonstrating that properties such as stellar age and sSFR are linked to the intrinsic $(u-r)_{\text{int}}$ colour. However, stellar-surface mass density also plays a significant role, particularly when distinguishing between blue and red regions.

We also used this diagram to explore the distribution of galaxy regions based on their colour and environment (see Fig. 3). We observe that regions of red and blue galaxies are distinctly separated, which is consistent with our previous findings, as seen in the radial profiles. Furthermore, the distribution of points is influenced not only by colour, but also by stellar mass density, since the division between regions of red and blue galaxies is traced by a diagonal line, and not just a vertical (stellar mass density) or horizontal (colour) line. Given the strong correlation between stellar mass density and radial distance (see, e.g. González Delgado et al. 2015, 2016; Bluck et al. 2020, and Sect. 4.2), we can consider stellar mass density as a proxy for the radial distance, at least to some extent. Consequently, these diagrams provide a different perspective on the colour profiles of galaxies.

No clear relation is found between galaxy environment and their position in these diagrams. The distribution of galaxies in groups is similar to that of galaxies in the field, with no noticeable clustering in specific regions. For a given mass-density bin, we find that the difference in the median $(u-r)_{\text{int}}$ colour of red galaxies between the field and groups is approximately 0.2–0.6 times the median uncertainty on the $(u-r)_{\text{int}}$ colour of red galaxies in that bin. For blue galaxies, this difference is slightly larger, ranging from 0.4 up to one times the typical uncertainty on the $(u-r)_{\text{int}}$ colour in the same regions; however, it still

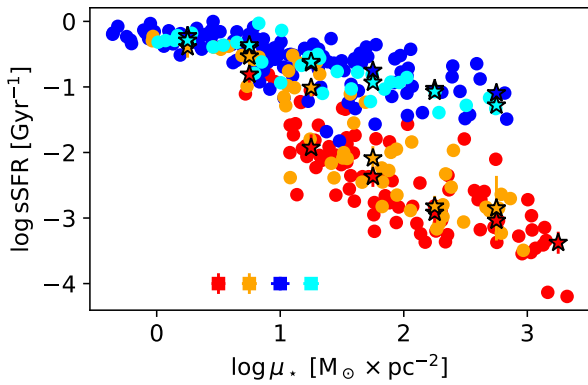


Fig. 4. Local star formation main sequence. Squares represent the typical error along each axis for each type of galaxy. Colour-coding is the same as in Fig. 3.

remains within the associated uncertainties. In the highest density bins, this difference is larger (up to twice the typical error), but the low number of points could be playing an important role in this difference. This result reflects our findings in the integrated analysis. In Rodríguez-Martín et al. (2022), we observed that the distribution of galaxy properties in the mass-colour diagram for the cluster mJPC2470-1771 was consistent with that of the general miniJPAS sample. The key difference was in the fraction of red and blue galaxies, which led to distinct clustering patterns. In contrast, our current results suggest that mass density and colour are more influential factors in the spatially resolved properties of galaxies than environment.

We conclude this section of our analysis of stellar-population properties by reproducing the local SFMS (see Fig. 4). Regions of red and blue galaxies are clearly separated. The difference of the sSFR for each mass-density bin is usually 0.4 to 0.7 times the typical error for said bin, so we do not find a significant effect of the environment on the blue galaxies in our sample in terms of this point. Regarding red galaxies, we find that the difference for a given mass-density bin is usually between the typical error and four times the typical error of that bin. This difference is statistically significant, but it is important to consider that, using the criteria of Peng et al. (2010), these regions are already quenched (their sSFR is lower than 0.1 Gyr^{-1}), so the actual value of the sSFR is less relevant. Our results are consistent with those of González Delgado et al. (2016), showing a strong relationship between the mass density of the region and its sSFR.

4.2. Radial distribution of the stellar-population properties

For the analysis of the radial distribution of the stellar-population properties, we used a fixed-step segmentation (see Fig. 5). As outlined in previous sections, we divided our sample into four groups based on environment and colour. Additionally, to facilitate comparison with existing literature, we assumed that red galaxies are typically quiescent and early types, while blue galaxies are generally star-forming and late types (see, e.g. Hogg et al. 2004; Kauffmann et al. 2004; Bassett et al. 2013). Although these categories are not synonymous, they are strongly correlated, making them a useful proxy for comparison purposes, as different studies often classify galaxies using varying criteria. After close inspection, we found that five red galaxies in the sample could be considered spirals, and one blue galaxy

could be considered an elliptical, but the PSF of the image makes the classification uncertain in some of these galaxies.

4.2.1. Stellar-mass surface density

Stellar mass density (top left panel in Fig. 5) decreases with increasing galactocentric radius for all galaxy spectral types and environments. Red galaxies in the field exhibit the highest densities, remaining above blue galaxies across all radii. At $0.7 R_{\text{EFF}}$, the median stellar mass density drops to $\log \mu_{\star} \approx 3$, with values consistent with previous studies (see, e.g. González Delgado et al. 2015; Bluck et al. 2020; Abdurro'uf et al. 2023; Conrado et al. 2024) but slightly lower due to PSF homogenisation and lower resolution in our radial bins. Differences between studies are attributed to varying stellar initial mass functions (IMFs), as the Salpeter IMF used in González Delgado et al. (2015) yields higher mass values than the Chabrier (2003) IMF used here (see also Díaz-García et al. 2024).

Red galaxies in groups have densities similar to those in the field, but ~ 0.1 dex lower. This difference remains between four and seven times larger than the typical error at each radii of the stellar mass surface density of red galaxies for all distances. These results align with Bluck et al. (2020), which found that satellite galaxies in groups are less dense than central galaxies, though high dispersion in group galaxy profiles warrants further investigation. Blue galaxies in both the field and groups show similar profiles; this is consistent with lower mass galaxies in previous studies and with findings by Bluck et al. (2020) and Abdurro'uf et al. (2023) for star-forming galaxies. The difference is between three and eight times the typical error of the stellar surface mass density of blue galaxies in central parts, but within the typical error at each radii for distances larger than $\sim 1 R_{\text{EFF}}$.

4.2.2. Stellar ages

Mass-weighted stellar ages (middle top panel in Fig. 5) exhibit similar profiles for red galaxies, whether in the field or in groups, remaining almost flat at $\langle \log \text{age} \rangle_M \approx 9.9$. Both types of red galaxies show a slight decrease in age up to $1 R_{\text{EFF}}$, followed by a slight increase, which is consistent with a rather flat profile. However, these trends fall within the uncertainty intervals, since the difference remains between 0.2 and 0.5 times the typical error at each radii of the age of the stellar ages of red galaxies, suggesting no significant environmental differences. Our findings align with previous studies that show a flat age profile for high-mass galaxies such as González Delgado et al. (2014, 2015) and San Roman et al. (2018).

Blue galaxies, in contrast, show more noticeable differences in their age profiles. In the field, age decreases from $\langle \log \text{age} \rangle_M \approx 9.5$ at $1 R_{\text{EFF}}$ to $\langle \log \text{age} \rangle_M \approx 9.4$ at $2 R_{\text{EFF}}$ and then increases again at larger radii. Blue galaxies in the field tend to be slightly younger than those in groups. This difference is larger for distances under $\sim 2 R_{\text{EFF}}$, where it is of the order 1–1.7 times the typical error at each radii of the age of blue galaxies. At larger radii, this difference is around 0.3 times the typical error, except for the last bin, where the lower number of points alters the final value. These results are consistent with previous studies, including González Delgado et al. (2014, 2015) and Bluck et al. (2020), where blue galaxies showed relatively flat age profiles, with younger populations at larger radii. We also observe that blue galaxies in groups are generally slightly more massive, but their age profiles remain similar across environments.

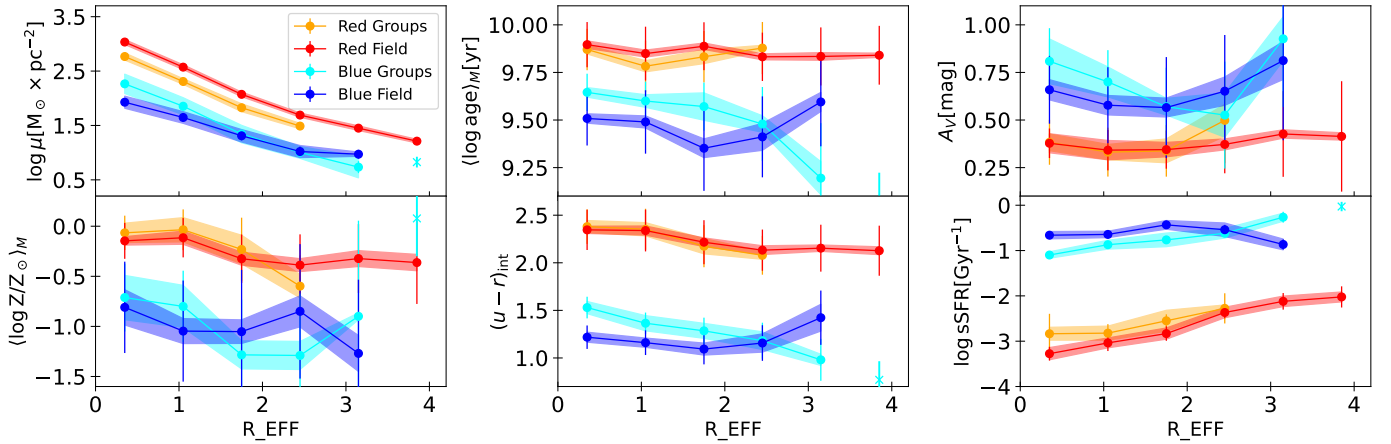


Fig. 5. Radial profile and gradients of stellar mass surface density by galaxy colour and environment. Colour-coding is the same as in Fig. 3. The dashed lines represent the median value in the radius bin. Each colour shade represents the error of the median. Error bars represent the typical error in each bin. Single points represent bins where only one region was left after the S/N cleaning.

4.2.3. Extinction

Extinction (right top panel in Fig. 5) shows a generally flat profile for red galaxies, both in groups and in the field, at around $A_V \approx 0.4$. In the field, red galaxies show a slight increase in A_V from $\sim 2 R_{\text{EFF}}$, but due to limited data at larger radii, this trend cannot be confirmed. Overall, no significant environmental effect on extinction is observed, likely due to measurement uncertainties. The difference remains between 0.04 and 0.8 times the typical error at each radii of the extinction of red galaxies. Our results are consistent with those of González Delgado et al. (2015), which observed a steep decrease in extinction up to $\sim 0.5 R_{\text{EFF}}$, followed by a flatter gradient. These findings also align with those of San Roman et al. (2018), which reported small positive gradients, with $A_V \approx [0.2, 0.5]$.

For blue galaxies, extinction decreases with radius in groups, from $A_V \approx 0.9$ in the central regions to $A_V \approx 0.5$ at $\sim 2.5 R_{\text{EFF}}$. This decrease correlates with the steep drop in mass-weighted age found for blue galaxies in groups, although the lack of data at larger radii suggests a possible degeneracy between age and extinction. In the field, extinction decreases from $A_V \approx 0.75$ at the centre to $A_V \approx 0.5$ at $\sim 2 R_{\text{EFF}}$, but without a steep change in age. While blue galaxies in groups tend to show slightly higher extinction, this difference is minimal between 0.02 and 0.9 times the typical error at each radii of the extinction of blue galaxies and may be related to mass distribution, as suggested by González Delgado et al. (2015). Our results show a similar pattern, with extinction decreasing in the inner regions of blue galaxies, generally ranging from $A_V \approx [0.4, 0.6]$. This is consistent with González Delgado et al. (2015), although we observe slightly higher extinction values.

4.2.4. Metallicity

Stellar mass-weighted metallicity profiles (bottom left panel in Fig. 5) decrease with radius for all galaxy types. For red galaxies in the field, metallicity drops from $\langle \log Z/Z_{\odot} \rangle \approx -0.25$ in the central regions to $\langle \log Z/Z_{\odot} \rangle \approx -0.5$ at $\sim 2 R_{\text{EFF}}$ and then remains constant in outer regions. Red galaxies in groups show a flatter metallicity profile up to $\sim 2 R_{\text{EFF}}$, though the uncertainty intervals make it difficult to confirm if environmental effects influence these profiles. These differences remain between 0.3 and 0.7 times the typical error at each radii of the metallicity

of red galaxies. compared with González Delgado et al. (2014, 2015), which reported a modest decrease in metallicity, our results show galaxies that are more metal-poor, which is consistent with the findings of San Roman et al. (2018). The discrepancies in metallicity are within expected uncertainty intervals and could arise from differences in methodology.

For blue galaxies, the metallicity profile is similar for both group and field galaxies, decreasing from $\langle \log Z/Z_{\odot} \rangle \approx -0.5$ at the centre to $\langle \log Z/Z_{\odot} \rangle \approx -1.25$ at $\sim 3 R_{\text{EFF}}$, with the drop potentially influenced by a degeneracy among stellar age, extinction, and metallicity. In the field, the profile shows a break around $\sim 2.5 R_{\text{EFF}}$, where the metallicity decrease slows. The difference between the metallicities of blue galaxies in the field and in groups remains between 0.2 and 0.7 times their typical error at each radius. If we compare our results with those by González Delgado et al. (2014, 2015), focusing on their galaxies within the mass range of $\log M_{\star} = [9.1, 10.6] [M_{\odot}]$, we find that the metallicity decreases with distance too, although at a slower rate. In fact, for their galaxies with masses of $\log M_{\star} < 10.1 [M_{\odot}]$, the profile looks rather flat, which results in a good agreement with our results.

4.2.5. Colour

The $(u-r)_{\text{int}}$ colour profiles (bottom middle panel in Fig. 5) clearly differentiate between red and blue galaxies. For red galaxies, the profiles are similar in both the field and groups, showing no significant environmental difference. In the central regions, red galaxies have $(u-r)_{\text{int}} \approx 2.4$, decreasing to $(u-r)_{\text{int}} \approx 2.1$ at $\sim 1.5 R_{\text{EFF}}$, after which they continue to decrease. In the field, the decrease begins at $\sim 1.2 R_{\text{EFF}}$, followed by a plateau. However, due to uncertainty intervals and differences in the number of galaxies in each environment, the environmental effect on colour is unclear. Nonetheless, the difference of their values remain between 0.06 and 0.26 times the typical error at each radii of the $(u-r)_{\text{int}}$ colour for red galaxies.

For blue galaxies, the colour profiles show more noticeable differences between the field and groups. In groups, $(u-r)_{\text{int}}$ decreases from ≈ 1.55 mag, becoming bluer more rapidly. In contrast, blue galaxies in the field exhibit a much flatter profile, with $(u-r)_{\text{int}} \approx 1.25$ mag at the centre, decreasing slightly

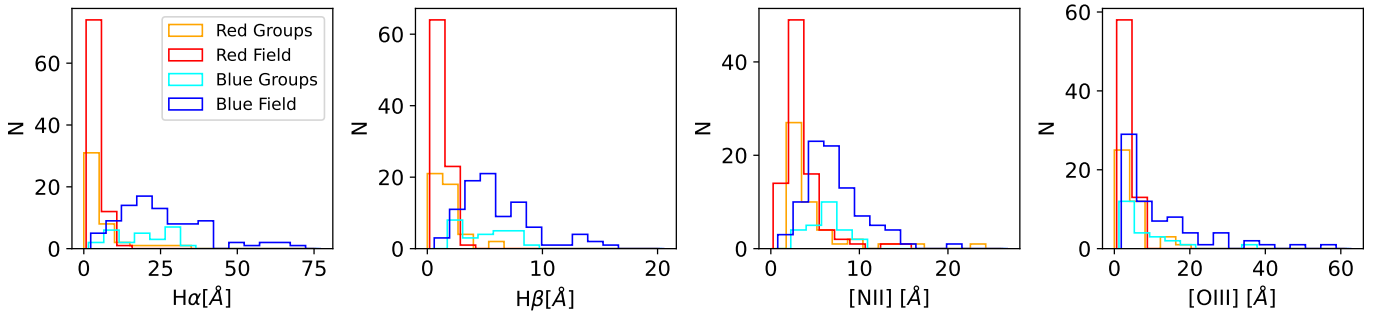


Fig. 6. Histograms of EW of line emission of regions of our sample of galaxies, by colour and environment. From left to right: EW($H\alpha$), EW($H\beta$), EW([NII]), and EW([OIII]). Colour-coding is the same as in previous figures.

to ~ 1.2 mag at $\sim 2 R_{\text{EFF}}$, and then increasing to ≈ 1.5 mag at $\sim 3 R_{\text{EFF}}$. This reddening at larger radii may be attributed to the fact that these outer regions can only be measured with sufficiently high S/Ns in more massive galaxies, which tend to be redder and more heavily obscured. The difference in colour between blue galaxies in the field and those in groups, which decreases from 2.5 to 0.25 times the typical error of $(u-r)_{\text{int}}$ at each radii, is not large enough to concretely link it to environmental effects, given the mass distribution of blue galaxies in the field, which skews towards more massive galaxies.

4.2.6. Specific star formation rate

We observed a clearly bimodal distribution in the radial profiles of the sSFR (bottom right panel in Fig. 5), dividing galaxies into red and blue populations. For red galaxies, the sSFR slightly increases with radial distance, both in the field and in groups. The profiles mostly overlap within the uncertainty, with differences ranging from one to two times the typical error at each radius of the sSFR of red galaxies. Values increasing from $\log \text{sSFR} \approx -3$ in the central regions to $\log \text{sSFR} \approx -2$ at $4 R_{\text{EFF}}$ for field galaxies and $\log \text{sSFR} \approx -2.5$ at $2.5 R_{\text{EFF}}$ for group galaxies. These profiles are consistent with those found by González Delgado et al. (2016) for elliptical and S0 galaxies, and Abdurro'uf et al. (2023) for quiescent galaxies. Red galaxies in both environments remain below the $\log \text{sSFR} = -1$ threshold adopted by Peng et al. (2010) to separate star-forming galaxies from quiescent systems, with negligible environmental differences.

Blue galaxies in the field exhibit flatter sSFR profiles at $\log \text{sSFR} \approx -0.85$, while those in groups show an increase from $\log \text{sSFR} \approx -1$ in the centre to $\log \text{sSFR} \approx 0$ at $4 R_{\text{EFF}}$. This increase may be flatter when considering other properties. Both blue galaxy populations exceeded the $\log \text{sSFR} = -1$ threshold from Peng et al. (2010), indicating active star formation. The sSFR of blue galaxies in the field appears slightly higher than that in groups, suggesting possible quenching in groups. The differences decrease from around nine times to 0.7 times the typical error at each bin of the sSFR of blue galaxies. These trends are consistent with previous studies, such as González Delgado et al. (2016) for Sc and Sd galaxies, and Abdurro'uf et al. (2023) for star-forming galaxies and those in the green valley. Our results align closely with the results of these studies, while Conrado et al. (2024) reported a quenched sSFR in the inner regions of high-mass spirals, which matches the flattening observed in our data.

4.3. Emission lines

In this section, we study the main predictions of the ANN for the regions we obtained with our methodology. We used the homogeneous rings' segmentation for the same reasons as in the previous section; i.e. in order to prevent higher resolution galaxies from dominating the radial profiles and colour-mass-density diagrams. We also analysed the BPT (Baldwin et al. 1981) and WHAN (Cid Fernandes et al. 2010, 2011) diagrams and separated star-forming regions and regions hosting and AGN.

4.3.1. Line emission of the regions

We begin our analysis of the emission lines by examining the distributions of EWs and line-emission ratios across galaxy regions in our sample, classified by colour and environment (see Fig. 6). We note that the median errors for these EWs are 4, 0.8, 1.5, and 2.76 Å for $H\alpha$, $H\beta$, [NII], and [OIII]. Given the limit of detection expressed by Eq. (6) from Martínez-Solaesche et al. (2021) (see also Pascual et al. 2007), most regions with an EW lower than 7.7, 9, 7.3, or 8.3 Å are compatible with no emission.

Red galaxies, both in the field and in groups, exhibit very low $H\alpha$ emission, with $\text{EW}(H\alpha) < 10$ Å. In contrast, blue galaxies show significantly stronger and more varied $H\alpha$ emission. For blue galaxies in groups, $\text{EW}(H\alpha)$ spans from a few Å up to ~ 30 Å, whereas in the field it extends to nearly ~ 75 Å, peaking at around 20 Å. The environment appears to have little effect on red galaxies, and the differences seen in blue galaxies may stem from variations in sample size. These trends are consistent with known correlations between stellar mass and $\text{EW}(H\alpha)$ (e.g. Fumagalli et al. 2012; Sobral et al. 2014; Khostovan et al. 2021). As $\text{EW}(H\alpha)$ traces SFR (Kennicutt 1998; Kennicutt & Evans 2012; Mármol-Queraltó et al. 2016; Khostovan et al. 2021), the higher values observed in blue galaxies align with their star-forming nature (e.g. Peng et al. 2010; Bluck et al. 2014) and our own findings of elevated SFR intensities in these regions.

Similar patterns are observed for $H\beta$. Red galaxies across environments display weak emission ($\text{EW}(H\beta) \approx 0-3$ Å), whereas blue galaxies exhibit stronger emission. In groups, blue galaxies show an $\text{EW}(H\beta)$ up to ~ 10 Å, and in the field this is up to ~ 17 Å, with a peak at 5 Å.

The distribution of [NII] emission shows subtle differences. Red galaxies still have relatively low $\text{EW}(\text{[NII]})$ values, though many regions have values above 0 Å, reaching up to ~ 15 Å. Blue galaxies generally show higher [NII] emission: group galaxies

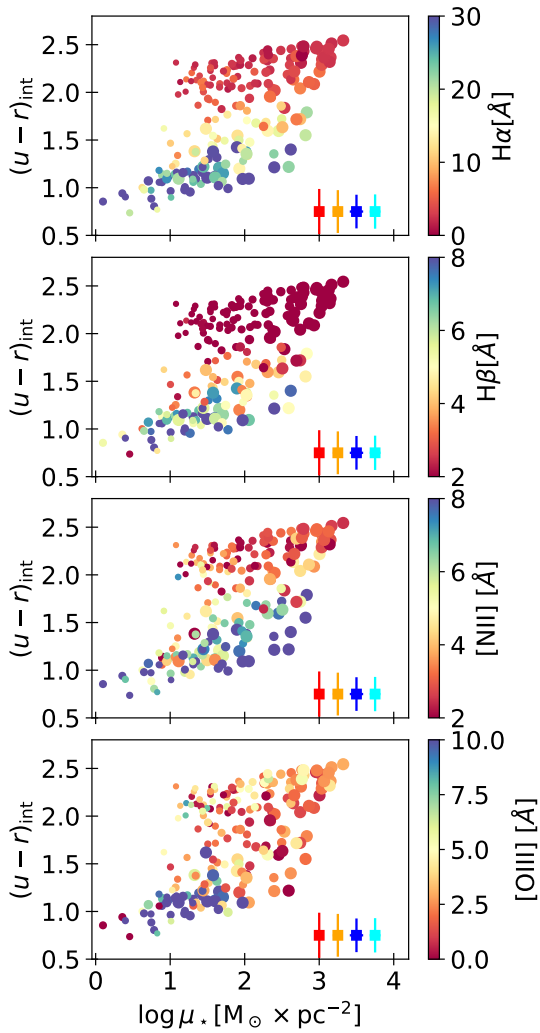


Fig. 7. Colour-mass-density diagram according to main stellar population properties. From top to bottom: EW($H\alpha$), EW($H\beta$), EW([NII]), and EW([OIII]). Squares represent the typical error along each axis colour for each type of galaxy.

range from ~ 1 to 10 \AA , while field galaxies extend up to 15 \AA , with both distributions peaking at around 5 \AA .

Finally, [OIII] emission also follows this pattern: red galaxies show weak emission ($0\text{--}10 \text{ \AA}$), while blue galaxies exhibit stronger [OIII] emission, particularly in the field (up to 60 \AA), and slightly lower emission in groups (up to 20 \AA).

The colour-mass-density diagram (see Fig. 7) provides a clear interpretation of the data, as both the EWs and line ratios exhibit well-defined distributions across the diagram. There is a strong correlation with galaxy colour, particularly in the case of the EWs of $H\alpha$ and $H\beta$. While this may be partly attributed to the fact that the ANNs are trained using colour information, there is also well-established evidence linking emission-line strength to galaxy colour classification (i.e. blue versus red galaxies; see, e.g. Martínez-Solaache et al. 2022, and references therein). Nonetheless, the influence of stellar mass surface density on emission properties should not be underestimated.

We observe that the EW of emission lines increases in blue regions with low stellar mass surface density. These regions also show the greatest variability in EW values. Based on earlier arguments using mass density as a proxy for galactocentric dis-

Table 1. Classification of central regions of galaxies in sample attending to the WHAN diagram.

Class	RG	RF	BG	BF
SF	0%	0%	66.67%	90.47%
Composite	44.44%	33.33%	33.33%	4.76%
Seyfert	0%	0%	0%	0%
LINER	11.11%	6.67%	0%	0%
Retired	44.4%	60%	0%	0%

Notes. Galaxies are divided by their spectral type and environment: red galaxies in groups (RG), red galaxies in the field (RF), blue galaxies in groups (BG), and blue galaxies in the field (BF).

tance, these areas correspond predominantly to the outer regions of blue galaxies. This variability is expected, as galaxies differ in their emission characteristics and include populations of extreme emission-line galaxies (see, e.g. Iglesias-Páramo et al. 2022, Martínez-Solaache et al. 2022, and references therein). Conversely, as regions become redder – particularly those with higher stellar mass densities – the EWs decrease markedly. These are typically the inner regions of red galaxies, which are generally quiescent and exhibit very low emission. The EW of [OIII], however, is only significant in low-density blue regions, and it diminishes rapidly elsewhere. It is important to note that our estimation of [OIII] emission is subject to greater uncertainty (Martínez-Solaache et al. 2021).

4.3.2. WHAN and BPT diagrams

We now analyse the BPT (Baldwin et al. 1981) and WHAN (Cid Fernandes et al. 2010, 2011) diagrams to classify regions as star forming or AGN dominated using our segmentation based on homogeneous ring analysis (see Fig. 8). We note that in the BPT, we only show regions above the retired line in the WHAN diagram; we did so in order to avoid biases and misclassifications produced by unreliable estimations in low- or no-emission-line regions. Regions belonging to blue galaxies are generally located within the star-forming area of both diagrams, although some fall into the ‘composite’ zone, lying between the demarcation lines proposed by Kauffmann et al. (2003) and Kewley et al. (2001). Only a small number of these regions appear in the LINER part of the diagrams, and we identify just one potential Seyfert region in the WHAN diagram and three in the BPT diagram.

In contrast, regions associated with red galaxies are predominantly found in the LINER and ‘retired’ areas of the WHAN diagram. In the BPT diagram, these regions tend to lie in the composite zone, with a greater number classified as Seyferts. It is important to note the lower accuracy in our estimation of the [OIII]/ $H\beta$ ratio, which affects the classification in the BPT diagram. Furthermore, we were unable to distinguish between galaxies in groups and those in the field based on these diagnostics.

To further investigate the role of the environment in triggering nuclear activity, we analysed the classifications obtained from the WHAN diagram for the innermost region of each galaxy (see Table 1). We focused on the WHAN diagram since it offers a better classification for low-emission galaxies given our filter system (see Martínez-Solaache et al. 2021, 2022). We used the maximum-resolution segmentation to delineate regions that enclose the innermost part of the galaxy. As before, these were classified according to their spectral type and environment.

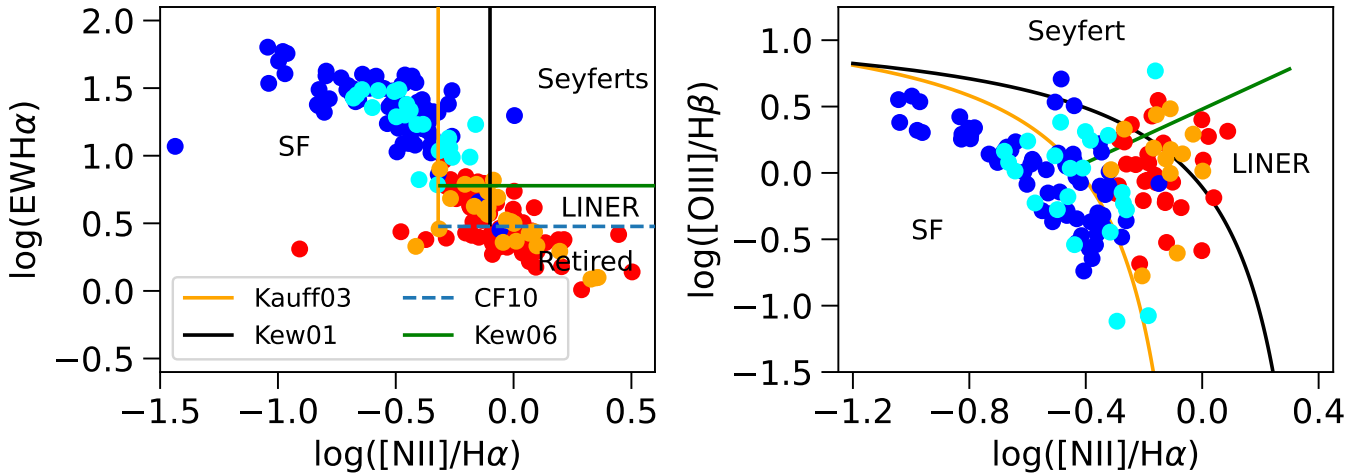


Fig. 8. WHAN (left panel) and BPT (right panel) diagrams of regions of spatially resolved galaxies in miniJPAS. Red points represent red galaxies in the field. Orange points represent red galaxies in groups. Blue points represent blue galaxies in the field. Cyan points represent blue galaxies in groups.

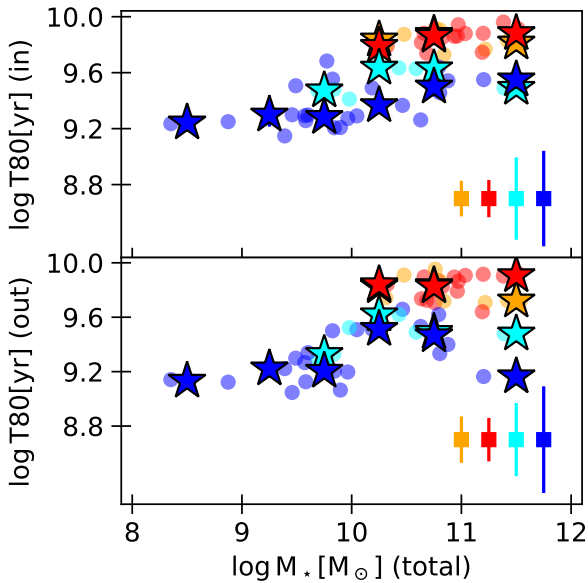


Fig. 9. T80 versus galaxy total mass. The upper panel shows the values for the inner region, while the bottom panel presents the values for the outer region. Colour-coding is the same as in previous figures. Stars represent the median value for each type of galaxy in each stellar mass bin. Squares represent the typical error along each axis colour for each type of galaxy.

We find that the percentage of AGN-host regions does not vary significantly between red galaxies in groups and red galaxies in the field. Conversely, we observe a higher percentage of nuclei in the composite regions of the diagrams for blue galaxies in groups compared with those in the field. Results from literature on this subject are mixed. For instance, [Peluso et al. \(2022\)](#) reported a strong correlation between AGN activity and ram-pressure stripping, which is more intense in denser environments, based on their optical sample. However, [Tiwari et al. \(2025\)](#) found no such correlation using an X-ray-based sample. Other studies, such as those by [Dressler et al. \(1985\)](#),

[Kauffmann et al. \(2004\)](#), and [Lopes et al. \(2017\)](#), observed a higher presence of AGNs in lower density environments, while works including [Amiri et al. \(2019\)](#) and [Muñoz Rodríguez et al. \(2024\)](#) did not find any significant relation with environment. In contrast, [de Vos et al. \(2024\)](#) reported a larger fraction of AGNs in the outskirts of clusters and in the very central regions, with a lower fraction in intermediate regions. Our previous work ([Rodríguez-Martín et al. 2022](#)) showed a higher fraction of AGN hosts in the core of the most massive cluster in miniJPAS. Our results suggest a scenario in which the environment does not play a significant role for red galaxies, but it does for blue galaxies. However, the scope of our conclusions is limited by the small sample size. A small statistical variation can lead to a considerable fluctuation in the reported AGN-host fraction. Therefore, our results should be regarded as a proof of concept and not generalised, as a larger sample would be necessary to either confirm or challenge this hypothesis.

4.4. SFH

We complete this section by studying the SFH of the galaxies. We used the inside-out segmentation, in order to compare the SFH of the inner and outer regions. We studied the parameter T80, which is the look-back time at which the galaxy has formed 80% of its stellar mass (taking into account the mass loss due to stars reaching the end of their lifetime). We show this parameter as a function of the total stellar mass, colour-coded according to the colour of the galaxy and its environment, in Fig. 9.

We find a strong correlation between T80 and stellar mass. Red, more massive galaxies exhibit higher T80 values in both inner and outer regions, indicating that these galaxies formed the bulk of their stars at earlier cosmological times. The similarity of T80 between the inner and outer regions suggests that star formation occurred over comparable timescales throughout the galaxy, within the precision limits of our stellar-population models.

Conversely, blue galaxies display lower T80 values, suggesting more recent star formation. These galaxies also show greater dispersion in the T80 values of their inner regions, which tend to be slightly higher than those in the outer regions. These differences are, however, really small: around 0.04 dex for red

galaxies and 0.07 dex for blue galaxies. These values are around 0.1 times the typical error of T80 for red galaxies and 0.2 times the typical error of T80 for blue galaxies. This result implies that blue galaxies may have formed their inner parts, possibly bulges, earlier than their outer discs, which is consistent with an inside-out growth scenario, as reported in several previous studies (see, e.g. Muñoz-Mateos et al. 2007; Pérez et al. 2013; Ibarra-Medel et al. 2016; Zheng et al. 2017; García-Benito et al. 2017), although the error budget is also compatible with a similar SFH for both parts.

The environment does not play a significant role in the differences in T80 between red galaxies, neither in the inner nor in the outer regions. For blue galaxies, we find some discrepancies: the inner regions of intermediate-mass blue galaxies ($\sim 10^{10} M_{\odot}$) in groups appear to have formed earlier than those of similar-mass galaxies in the field.

5. Discussion

Throughout this work, we found radial profiles of the stellar-population properties that are in agreement with the literature, particularly (but not exclusively) the works of González Delgado et al. (2014, 2015, 2016), San Roman et al. (2018), Bluck et al. (2020), Parikh et al. (2021), and Abdurro'uf et al. (2023), and, from a certain perspective, our results mirror the well-established integrated properties of galaxies. Red galaxies are generally more massive, older, and more metal-rich, and they exhibit lower SFRs and sSFRs than blue galaxies. Our results show that this behaviour also holds on local scales: regions belonging to red galaxies are typically redder, older, and more metal-rich, and they have higher stellar mass surface densities and display lower sSFR than regions in blue galaxies at the same galactocentric distance. The profiles show clear differences between red and blue galaxies, but no significant difference between galaxies in the field and in groups. We note here that we were limited by several factors. The first one and probably the most important of these is that our sample of galaxies is quite small. The results themselves for each galaxy are trustworthy because of our selection and because of the proofs performed in Rodríguez-Martín et al. (2025), but their statistical significance will improve once more data become available. Another factor is that our selection of galaxies is limited to galaxy groups, which usually have lower masses than clusters. This is important because the efficiency of several environment-related processes increases with the mass of the group or cluster (Alonso et al. 2012; Raj et al. 2019). In particular, the range of the total stellar mass of groups, which is related to total mass, is $\sim 10^{10.25} - 10^{11.5} M_{\odot}$ for groups containing our blue galaxies, and $\sim 10^{10.75} - 10^{12} M_{\odot}$ for groups containing our red galaxies. This mass range is significantly lower than the total stellar mass of the galaxy cluster studied in Rodríguez-Martín et al. (2022), which is around $10^{12.5} M_{\odot}$. In relation to this point, in González Delgado et al. (2022) we found differences between the integrated properties of galaxies in groups and in the field, but many of these differences were due to the fraction of red and blue galaxies, and the properties of galaxies with the same mass and colour also showed similar properties, regardless of their environment, similarly to the results found here. Lastly, the resolution of the binning of the galaxy affects the profile: a lower spatial resolution results in a flatter profile. Therefore, we may be able to produce profiles with better resolution showing more significant differences in the future, when data of galaxies with larger apparent sizes become available.

In general, we find that, due to their masses, red and blue galaxies are largely well separated in the various diagrams analysed in this paper. However, similarly to the case of the radial profiles, we observe no significant differences between group and field galaxies. Regarding the results related to the gradients of the stellar population properties, the two galaxies in our sample with masses below $10^9 M_{\odot}$ are distinct from the rest, and, when they are considered as outliers, we can identify some trends in the gradients in relation to galaxy stellar mass.

Concerning the role of environment on galaxy evolution, it is common to compare it to the role of the stellar mass, as reflected by the division of the quenching process into mass quenching and environmental quenching (e.g. Peng et al. 2010; Ilbert et al. 2013). In fact, the radial profiles of stellar population properties studied by González Delgado et al. (2015) show a dependence not only on the morphological type of the galaxy, but also on its total stellar mass, as well as the galaxies studied by Conrado et al. (2024). Furthermore, Zibetti & Gallazzi (2022) pointed to the stellar mass as both a local and global driver of the evolution of galaxies. For this reason, we decided to include the radial profiles of the stellar-population properties previously studied, but divided into mass bins (see Fig. 10).

We find that, for most properties, their values are distinct in terms of mass at all distances. In particular, the stellar mass surface density is always higher for massive galaxies than for low-mass galaxies, and massive galaxies are older, more metal-rich, and redder at all distances compared to low-mass galaxies. Additionally, the profiles of the sSFR also show clear offsets with mass, where low-mass galaxies have significantly higher sSFR than massive galaxies. The most notable exception is extinction, which shows similar profiles across all masses. On the other hand, the radial profiles of the intensity of the SFR are almost bimodal, with galaxies in the range of $M_{\star} = [10^8, 10^{10.5}] M_{\odot}$ showing comparable profiles within the uncertainty intervals; however, they are still clearly distinguished from galaxies with masses larger than $10^{10.5} M_{\odot}$. These results show that the mass indeed plays a significant role in the determination of the local properties of galaxies, as found in the aforementioned works. However, we also point out that the mass of our groups may be too low for the environment to exert any significant effect in our spatially resolved galaxies. Indeed, the mass of the groups in miniJPAS is very low in comparison to massive clusters, as shown by González Delgado et al. (2022). In that work, we showed how the quenched fraction excess of galaxies was significantly higher for the cluster mJPC2470-1771 than for low-mass groups. Therefore, we may see more significant effects in the properties of the spatially resolved galaxies in groups and clusters with higher masses in the future data releases of miniJPAS.

6. Summary and conclusions

We applied our tool, Py2DJPAS, to the spatially resolved galaxies from the miniJPAS survey in order to study the effect of the environment on the spatially resolved properties of 51 galaxies in miniJPAS. We checked the observational and the integrated properties of the sample, checking that red galaxies in the field and in groups are comparable among them, as well as blue galaxies in the field and in groups, but we had to take into account that the sample of blue galaxies in the groups is biased towards higher masses.

In the spatially resolved analysis, we mainly used semi-major-axis elliptical rings the size of the FWHM of the worst PSF for each galaxy, and elliptical rings of $0.7 R_{\text{EFF}}$. We

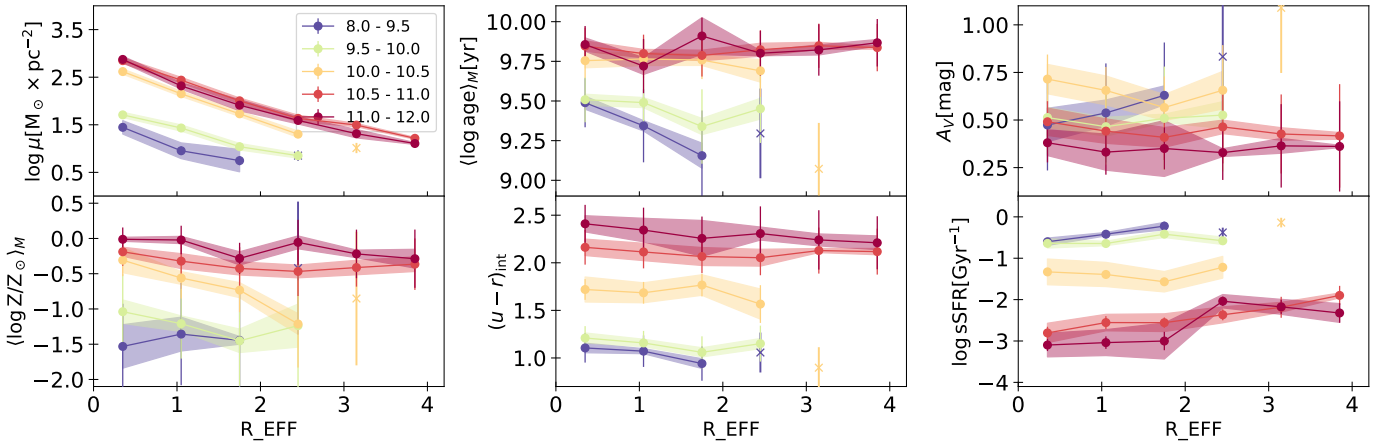


Fig. 10. Radial profiles of stellar-population properties, divided by mass bins. From left to right, top to bottom: stellar mass surface density, mass-weighted age, extinction, stellar metallicity, $(u-r)_{\text{int}}$ colour, and sSFR. Different colours represent mass bins. The dashed lines represent the median value in each mass bin; shades represent the error of the median, the error bars represent the typical error in each bin, and single points represent radius bins with only one region.

studied the stellar-population and emission-line properties of these regions, using a mass density–colour diagram and their radial profiles and gradients. Lastly, we compared the SFH from the inside to the outside of galaxies, using elliptical rings defined from the centre up to $0.7 R_{\text{EFF}}$ for inner regions, and from $0.7 R_{\text{EFF}}$ to $2.5 R_{\text{EFF}}$. Our main conclusions are listed below.

- Our tool, Py2DJPAS, provides solid magnitude measurements that offer reliable galaxy properties.
- The properties of the regions are clearly distributed in the colour-mass-density, similarly to the integrated mass-colour diagram. We find that redder, denser regions are usually older, more metal rich, and show lower values of the sSFR (they are more quiescent) than bluer, less dense regions. The highest values of the extinction, A_V , are found in blue, dense regions, as well as some of the most metal-rich regions. The regions of red and blue galaxies remain clearly separated in these diagrams.
- The radial profiles of the properties of the galaxies that we obtained are compatible with extensive examples from literature. The profiles of the red and blue galaxies are clearly different, but we do not find any remarkable effect of the environment.
- The EWs of emission lines vary across the colour-mass-density diagram, with the highest EWs in the bluest, least dense regions. WHAN and BPT diagrams show that blue galaxy regions are mostly star forming, whereas red galaxy regions are classified as LINERs or retired.
- The comparison of the SFH of the inner and outer regions suggests an inside-outside formation scenario.
- We find that in general, the properties of the regions of red and blue galaxies are well distinguished, but that there is no significant effect of the environment in the properties of these regions.

Acknowledgements. J.E.R.M., L.A.D.G., R.M.G.D., G.M.S., R.G.B., and I.M. acknowledge financial support from the Severo Ochoa grant CEX2021-001131-S funded by MICIU/AEI/ 10.13039/501100011033. J.E.R.M., L.A.D.G., R.M.G.D., G.M.S., and R.G.B., are also grateful for financial support from the project PID2022-141755NB-I00, and proyect ref. AST22_00001_Subp 12 and 11 with fundings from the European Union – NextGenerationEU; the Ministerio de Ciencia, Innovación y Universidades; the Plan de Recuperación, Transformación y Resiliencia; the Consejería de Universidad, Investigación e Innovación from the Junta de Andalucía and the Consejo Superior de Inves-

tigaciones Científicas. I.M. acknowledges financial support from the project PID2022-140871NB-C21 Based on observations made with the JST/T250 telescope and PathFinder camera for the miniJPAS project at the Observatorio Astrofísico de Javalambre (OAJ), in Teruel, owned, managed, and operated by the Centro de Estudios de Física del Cosmos de Aragón (CEFCA). We acknowledge the OAJ Data Processing and Archiving Unit (UPAD) for reducing and calibrating the OAJ data used in this work. Funding for OAJ, UPAD, and CEFCA has been provided by the Governments of Spain and Aragón through the Fondo de Inversiones de Teruel; the Aragón Government through the Research Groups E96, E103, E16_17R, and E16_20R; the Spanish Ministry of Science, Innovation and Universities (MCIU/AEI/FEDER, UE) with grant PGC2018-097585-B-C21; the Spanish Ministry of Economy and Competitiveness (MINECO/FEDER, UE) under AYA2015-66211-C2-1-P, AYA2015-66211-C2-2, AYA2012-30789, and ICTS-2009-14; and European FEDER funding (FCDD10-4E-867, FCDD13-4E-2685). This paper has gone through internal review by the J-PAS collaboration. We thank Gustavo Bruzual for his work as an internal referee, as well as Iris Breda and Álvaro Álvarez Candal for their comments to improve the paper.

References

- Abdurro'uf, Coe, D., Jung, I., et al. 2023, *ApJ*, **945**, 117
Alonso, S., Mesa, V., Padilla, N., & Lambas, D. G. 2012, *A&A*, **539**, A46
Amiri, A., Tavasoli, S., & De Zotti, G. 2019, *ApJ*, **874**, 140
Bacon, R., Copin, Y., Monnet, G., et al. 2001, *MNRAS*, **326**, 23
Baldwin, J. A., Phillips, M. M., & Terlevich, R. 1981, *PASP*, **93**, 5
Bassett, R., Papovich, C., Lotz, J. M., et al. 2013, *ApJ*, **770**, 58
Bell, E. F., & de Jong, R. S. 2000, *MNRAS*, **312**, 497
Bellagamba, F., Maturi, M., Hamana, T., et al. 2011, *MNRAS*, **413**, 1145
Bellagamba, F., Roncarelli, M., Maturi, M., & Moscardini, L. 2018, *MNRAS*, **473**, 5221
Benitez, N., Dupke, R., Moles, M., et al. 2014, arXiv e-prints [arXiv:1403.5237]
Bertin, E., Mellier, Y., Radovich, M., et al. 2002, *ASP Conf. Ser.*, **281**, 228
Bluck, A. F. L., Mendel, J. T., Ellison, S. L., et al. 2014, *MNRAS*, **441**, 599
Bluck, A. F. L., Maiolino, R., Piotrowska, J. M., et al. 2020, *MNRAS*, **499**, 230
Bonoli, S., Marín-Franch, A., Varela, J., et al. 2021, *A&A*, **653**, A31
Bruzual, G., & Charlot, S. 2003, *MNRAS*, **344**, 1000
Bundy, K., Bershady, M. A., Law, D. R., et al. 2015, *ApJ*, **798**, 7
Calzetti, D., Armus, L., Bohlin, R. C., et al. 2000, *ApJ*, **533**, 682
Cappellari, M., Emsellem, E., Krajnović, D., et al. 2011, *MNRAS*, **413**, 813
Cenarro, A. J., Moles, M., Marín-Franch, A., et al. 2014, *SPIE Conf. Ser.*, **9149**, 914911
Cenarro, A. J., Moles, M., Cristóbal-Hornillos, D., et al. 2019, *A&A*, **622**, A176
Chabrier, G. 2003, *PASP*, **115**, 763
Cid Fernandes, R., Stasińska, G., Schlickmann, M. S., et al. 2010, *MNRAS*, **403**, 1036
Cid Fernandes, R., Stasińska, G., Mateus, A., & Vale Asari, N. 2011, *MNRAS*, **413**, 1687
Conrado, A. M., González Delgado, R. M., García-Benito, R., et al. 2024, *A&A*, **687**, A98
Cypriano, E. S., Amara, A., Voigt, L. M., et al. 2010, *MNRAS*, **405**, 494

- Darnell, T., Bertin, E., Gower, M., et al. 2009, *ASP Conf. Ser.*, **411**, 18
- de Vos, K., Hatch, N. A., & Merrifield, M. R. 2024, *MNRAS*, **535**, 217
- Desai, S., Armstrong, R., Mohr, J. J., et al. 2012, *ApJ*, **757**, 83
- Díaz-García, L. A., Cenarro, A. J., López-Sanjuan, C., et al. 2019a, *A&A*, **631**, A156
- Díaz-García, L. A., Cenarro, A. J., López-Sanjuan, C., et al. 2019b, *A&A*, **631**, A158
- Díaz-García, L. A., González Delgado, R. M., García-Benito, R., et al. 2024, *A&A*, **688**, A113
- Doubrawa, L., Cypriano, E. S., Finoguenov, A., et al. 2023, *MNRAS*, **526**, 4285
- Dressler, A., Thompson, I. B., & Shectman, S. A. 1985, *ApJ*, **288**, 481
- Fumagalli, M., Patel, S. G., Franx, M., et al. 2012, *ApJ*, **757**, L22
- García-Benito, R., González Delgado, R. M., Pérez, E., et al. 2017, *A&A*, **608**, A27
- Goddard, D., Thomas, D., Maraston, C., et al. 2017, *MNRAS*, **466**, 4731
- González Delgado, R. M., Cerviño, M., Martins, L. P., Leitherer, C., & Hauschildt, P. H. 2005, *MNRAS*, **357**, 945
- González Delgado, R. M., Pérez, E., Cid Fernandes, R., et al. 2014, *A&A*, **562**, A47
- González Delgado, R. M., García-Benito, R., Pérez, E., et al. 2015, *A&A*, **581**, A103
- González Delgado, R. M., Cid Fernandes, R., Pérez, E., et al. 2016, *A&A*, **590**, A44
- González Delgado, R. M., Díaz-García, L. A., de Amorim, A., et al. 2021, *A&A*, **649**, A79
- González Delgado, R. M., Rodríguez-Martín, J. E., Díaz-García, L. A., et al. 2022, *A&A*, **666**, A84
- Hernán-Caballero, A., Varela, J., López-Sanjuan, C., et al. 2021, *A&A*, **654**, A101
- Hogg, D. W., Blanton, M. R., Brinchmann, J., et al. 2004, *ApJ*, **601**, L29
- Ibarra-Medel, H. J., Sánchez, S. F., Avila-Reese, V., et al. 2016, *MNRAS*, **463**, 2799
- Iglesias-Páramo, J., Arroyo, A., Kehrig, C., et al. 2022, *A&A*, **665**, A95
- Ilbert, O., McCracken, H. J., Le Fèvre, O., et al. 2013, *A&A*, **556**, A55
- Kauffmann, G., Heckman, T. M., Tremonti, C., et al. 2003, *MNRAS*, **346**, 1055
- Kauffmann, G., White, S. D. M., Heckman, T. M., et al. 2004, *MNRAS*, **353**, 713
- Kennicutt, R. C., Jr. 1998, *ARA&A*, **36**, 189
- Kennicutt, R. C., & Evans, N. J. 2012, *ARA&A*, **50**, 531
- Kewley, L. J., Dopita, M. A., Sutherland, R. S., Heisler, C. A., & Trevena, J. 2001, *ApJ*, **556**, 121
- Khostovan, A. A., Malhotra, S., Rhoads, J. E., et al. 2021, *MNRAS*, **503**, 5115
- Liao, L.-W., & Cooper, A. P. 2023, *MNRAS*, **518**, 3999
- Lin, L., Hsieh, B.-C., Pan, H.-A., et al. 2019, *ApJ*, **872**, 50
- Logroño-García, R., Vilella-Rojo, G., López-Sanjuan, C., et al. 2019, *A&A*, **622**, A180
- Lopes, P. A. A., Ribeiro, A. L. B., & Rembold, S. B. 2017, *MNRAS*, **472**, 409
- Madau, P., Pozzetti, L., & Dickinson, M. 1998, *ApJ*, **498**, 106
- Marín-Franch, A., Taylor, K., Santoro, F. G., et al. 2017, in *Highlights on Spanish Astrophysics IX*, eds. S. Arribas, A. Alonso-Herrero, F. Figueras, et al., 670
- Mármol-Queraltó, E., McLure, R. J., Cullen, F., et al. 2016, *MNRAS*, **460**, 3587
- Martínez-Solaache, G., González Delgado, R. M., García-Benito, R., et al. 2021, *A&A*, **647**, A158
- Martínez-Solaache, G., González Delgado, R. M., García-Benito, R., et al. 2022, *A&A*, **661**, A99
- Martínez-Solaache, G., Queiroz, C., González Delgado, R. M., et al. 2023, *A&A*, **673**, A103
- Maturo, M., Meneghetti, M., Bartelmann, M., Dolag, K., & Moscardini, L. 2005, *A&A*, **442**, 851
- Maturi, M., Finoguenov, A., Lopes, P. A. A., et al. 2023, *A&A*, **678**, A145
- Mendes de Oliveira, C., Ribeiro, T., Schoenell, W., et al. 2019, *MNRAS*, **489**, 241
- Michard, R. 2002, *A&A*, **384**, 763
- Moles, M., Aguerri, J. A. L., Alfaro, E. J., et al. 2008, *ASP Conf. Ser.*, **390**, 495
- Molino, A., Benítez, N., Moles, M., et al. 2014, *MNRAS*, **441**, 2891
- Muñoz Rodríguez, I., Georgakakis, A., Shankar, F., et al. 2024, *MNRAS*, **532**, 336
- Muñoz-Mateos, J. C., Gil de Paz, A., Boissier, S., et al. 2007, *ApJ*, **658**, 1006
- Oke, J. B., & Gunn, J. E. 1983, *ApJ*, **266**, 713
- Parikh, T., Thomas, D., Maraston, C., et al. 2021, *MNRAS*, **502**, 5508
- Pascual, S., Gallego, J., & Zamorano, J. 2007, *PASP*, **119**, 30
- Peluso, G., Vulcani, B., Poggianti, B. M., et al. 2022, *ApJ*, **927**, 130
- Peng, Y.-J., Lilly, S. J., Kovač, K., et al. 2010, *ApJ*, **721**, 193
- Pérez, E., Cid Fernandes, R., González Delgado, R. M., et al. 2013, *ApJ*, **764**, L1
- Planck Collaboration VI. 2020, *A&A*, **641**, A6
- Plat, A., Charlot, S., Bruzual, G., et al. 2019, *MNRAS*, **490**, 978
- Queiroz, C., Abramo, L. R., Rodrigues, N. V. N., et al. 2023, *MNRAS*, **520**, 3476
- Rahna, P. T., Akhlaghi, M., López-Sanjuan, C., et al. 2025, *A&A*, **695**, A200
- Raj, M. A., Iodice, E., Napolitano, N. R., et al. 2019, *A&A*, **628**, A4
- Rodrigues, N. V. N., Raul Abramo, L., Queiroz, C., et al. 2023, *MNRAS*, **520**, 3494
- Rodríguez-Martín, J. E., González Delgado, R. M., Martínez-Solaache, G., et al. 2022, *A&A*, **666**, A160
- Rodríguez-Martín, J. E., Díaz-García, L. A., González Delgado, R. M., et al. 2025, *A&A*, **704**, A52
- San Roman, I., Cenarro, A. J., Díaz-García, L. A., et al. 2018, *A&A*, **609**, A20
- Sánchez, S. F. 2020, *ARA&A*, **58**, 99
- Sánchez, S. F., Kennicutt, R. C., Gil de Paz, A., et al. 2012, *A&A*, **538**, A8
- Sánchez, S. F., Walcher, C. J., Lopez-Cobá, C., et al. 2021, *Rev. Mex. Astron. Astrofis.*, **57**, 3
- Schaefer, A. L., Tremonti, C., Pace, Z., et al. 2019, *ApJ*, **884**, 156
- Sobral, D., Best, P. N., Smail, I., et al. 2014, *MNRAS*, **437**, 3516
- Tanaka, T. S., Shimasaku, K., Tacchella, S., et al. 2024, *PASJ*, **76**, 1
- Taylor, K., Marín-Franch, A., Laporte, R., et al. 2014, *J. Astron. Instrum.*, **3**, 1350010
- Tiwari, J., Sun, M., Luo, R., et al. 2025, *ApJ*, **979**, 134
- Trayford, J. W., Theuns, T., Bower, R. G., et al. 2016, *MNRAS*, **460**, 3925
- Yang, X., Mo, H. J., van den Bosch, F. C., et al. 2007, *ApJ*, **671**, 153
- Yang, X., Mo, H. J., & van den Bosch, F. C. 2009, *ApJ*, **695**, 900
- Zheng, Z., Wang, H., Ge, J., et al. 2017, *MNRAS*, **465**, 4572
- Zibetti, S., & Gallazzi, A. R. 2022, *MNRAS*, **512**, 1415

-
- ¹ Instituto de Astrofísica de Andalucía (IAA-CSIC), P.O. Box 3004, 18080 Granada, Spain
 - ² Departamento de Física, Universidade Federal de Santa Catarina, P.O. Box 476, 88040-900 Florianópolis, SC, Brazil
 - ³ University of Heidelberg, Heidelberg, Germany
 - ⁴ Instituto de Física de Cantabria (CSIC-UC), Avda. Los Castros s/n, 39005 Santander, Spain
 - ⁵ Unidad Asociada “Grupo de Astrofísica Extragaláctica y Cosmología”, IFCA-CSIC/Universitat de València, València, Spain
 - ⁶ Instituto de Física, Universidade de São Paulo, Rua do Matão 1371, CEP 05508-090 São Paulo, Brazil
 - ⁷ Observatório Nacional – MCTI (ON), Rua Gal. José Cristino 77, São Cristóvão, 20921-400 Rio de Janeiro, Brazil
 - ⁸ Donostia International Physics Center (DIPC), Manuel Lardizabal Ibilbidea 4, San Sebastián, Spain
 - ⁹ IKERBASQUE, Basque Foundation for Science, 48013 Bilbao, Spain
 - ¹⁰ Centro de Estudios de Física del Cosmos de Aragón (CEFCA), Unidad Asociada al CSIC Plaza San Juan 1, 44001 Teruel, Spain
 - ¹¹ Centro de Estudios de Física del Cosmos de Aragón (CEFCA), Plaza San Juan 1, 44001 Teruel, Spain
 - ¹² Instituto de Astrofísica de Canarias (IAC), C/ Vía Láctea, S/N, E-38205 San Cristóbal de La Laguna, Tenerife, Spain
 - ¹³ Departamento de Astrofísica, Universidad de La Laguna (ULL), Avenida Francisco Sánchez, E-38206 San Cristóbal de La Laguna, Tenerife, Spain
 - ¹⁴ Universidade de São Paulo, Instituto de Astronomia, Geofísica e Ciências Atmosféricas, Rua do Maão 1226, 05508-090 São Paulo, Brazil
 - ¹⁵ Instruments4, 4121 Pembury Place, La Canada Flintridge, CA 91011, USA

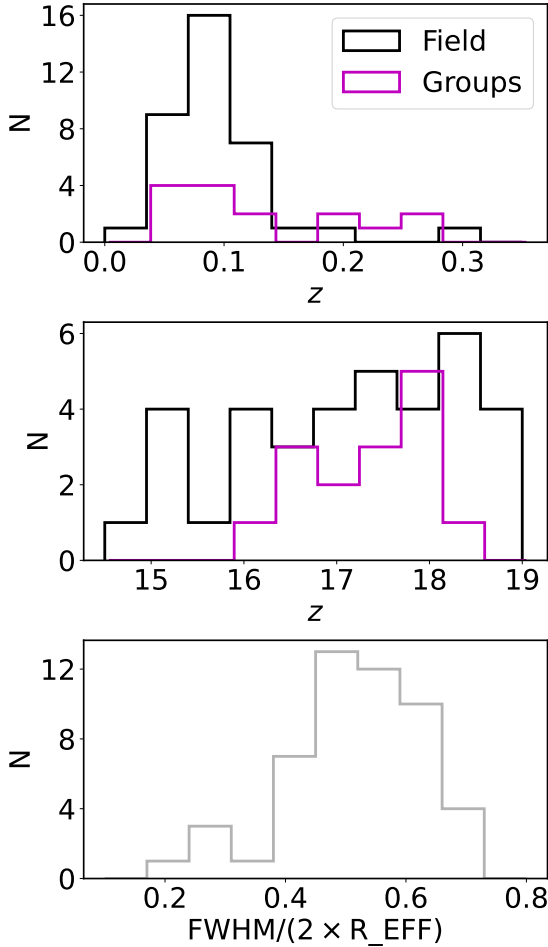


Fig. A.1. Integrated observational properties of the spatially resolved galaxies in this work. First panel shows the histogram of the redshift of the galaxies. Middle panel shows the distribution of the magnitude in the r_{SDSS} of the MAG_AUTO photometry. Black histograms represent galaxies in the field, and magenta histograms represent galaxies in groups. Last panel shows the comparison of the FWHM of the worst PSF for each galaxy and the double of its effective radius for the complete sample.

Appendix A: Observational and integrated properties of the sample

In this appendix we summarise the main observational (Fig. A.1) and integrated (Fig. A.2) properties of the sample of galaxies. We compare these properties to avoid biases and wrong conclusions in our analysis when analysing the role of environment on galaxy evolution.

The most important aspect of the comparison of the observational properties (Fig. A.1) is that galaxies in groups and in the field cover a similar redshift range, which ensures a fair comparison between properties of both types of galaxies. We also find that there are brighter and also dimmer galaxies in the field than in groups, but this is most likely due to the different size of the samples. Lastly, the last panel of Fig. A.1 shows the comparison of the R_EFF of each galaxy to the FWHM of its worst PSF, justifying our choice of steps of $0.7 R_{EFF}$ during our analysis.

Regarding the integrated stellar population properties (Fig. A.2), we find that red galaxies have very similar distributions regardless of their environment. However, we find that our sample of blue galaxies in groups is biased towards larger values

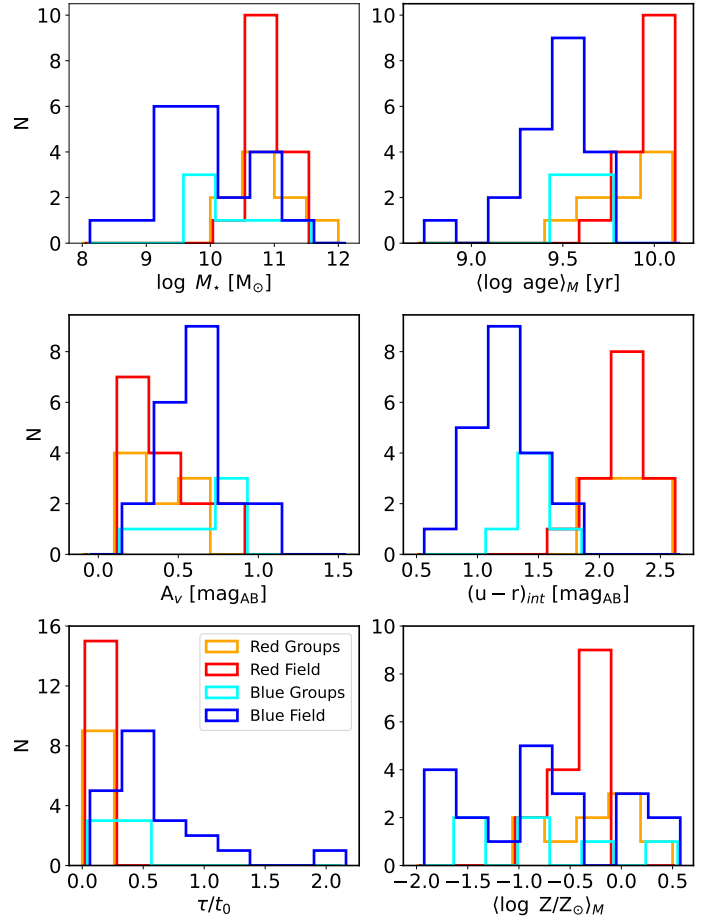


Fig. A.2. Comparison of the integrated stellar population properties of the spatially resolved galaxies by colour and environment. From left to right, top to bottom: stellar mass, mass-weighted age, extinction A_V , $(u-r)_{int}$, τ/t_0 , and stellar metallicity. Colour code is the same as in previous figures

of the mass and older values of the age. This also means redder values of the $(u-r)_{int}$ colour, as well as lower values of τ/t_0 indicating shorter star formation episodes. These differences may be caused by the size of the sample, but it is important to take them into account during the analysis of the spatially resolved properties.